Science Advances
AAAS

Supplementary Materials for

Underwater metamaterial absorber with impedance-matched composite

Sichao Qu, Nan Gao, Alain Tinel, Bruno Morvan, Vicente Romero-García, Jean-Philippe Groby, Ping Sheng*

*Corresponding author. Email: sheng@ust.hk

Published 18 May 2022, *Sci. Adv.* **8**, eabm4206 (2022)
DOI: 10.1126/sciadv.abm4206

This PDF file includes:

Text S1. The single Fabry-Perot resonator

We develop an integration scheme involving higher-order resonances so as to obtain the lengths recipe $(L_1, L_2, \ldots, L_N)$ for broadband impedance matching. To begin with, the acoustic pressure and velocity in the composite rod with length L_n, can be written as

$$\begin{cases} u(z) = u_0 \sin\left[\omega\left(z + L_n\right)\sqrt{\rho_c / M}\right] \\ p(z) = iZ_w u_0 \cos\left[\omega\left(z + L_n\right)\sqrt{\rho_c / M}\right] \end{cases}, \tag{S1}$$

where u denotes the displacement velocity, u_0 being its magnitude, $z = 0$ is defined to be the top surface of the Fabry-Perot (FP) resonator, and the longitudinal modulus $M \cong E_c(1 - i\eta) =$

$B_w(1-i\eta)/\alpha$, with $\alpha = 5.5$ in our present case. We will show in the following section that the loss factor $\eta \cong 0.26$.

The composite material's characteristic impedance Z_c is assumed to be matched to that of water, Z_w. Note that we define the material properties as $\rho_c = \alpha\rho_w$, $v_c = v_w/\alpha$ and $Z_w = \rho_c v_c = \rho_w v_w$. The water's density $\rho_w = 1\ \mathrm{g/cm^3}$ and sound speed $v_w = 1470\ \mathrm{m/s}$. E_c is the Young's modulus of the composite rod, B_w is the bulk modulus of water. The surface impedance of a single FP resonator, let us say the n_{th} resonator in the integrated array, is defined by

$$Z_n = \frac{p(0)}{u(0)} = iZ_w \cot\left(\frac{\omega L_n}{v_c}\right), \tag{S2}$$

where the sound speed $v_c = \sqrt{M/\rho_c}$. The first-order Fabry-Perot (FP) resonance occurs when the longitudinal length coincidences the quarter wavelength $L_n = \lambda/4$. It should be noted that since M can have a small imaginary part, the relevant v_c is also complex in the simulations. Only the real part of M is taken into account in the impedance matching considerations.

Higher-order resonances happen when the relevant wavelength is shorter so that $L_n = 3\lambda/4, 5\lambda/4, \ldots, (2m-1)\lambda/4$ are satisfied ($m > 1$). By using the Mittag-Leffler expansion:

$$\tan\left[\frac{\pi x}{2}\right] = \frac{4x}{\pi}\sum_{m=1}^{\infty}\frac{1}{(2m-1)^2 - x^2}\ , \tag{S3}$$

we can alternately express Eq. (S2) as

$$Z_n = -\frac{1}{i\omega G_n} = -\frac{1}{i\omega}\left(\sum_{m=1}^{\infty}\frac{\chi_n}{(2m-1)^2\Omega_n^2 - \omega^2 - i\beta\omega}\right)^{-1}, \tag{S4}$$

where the Green function, G_n, is defined to be the ratio of surface displacement to the pressure modulation ($= u/-i\omega$), m denotes the order of the FP resonance, the oscillation strength $\chi_n = 2/(\alpha\rho_w L_n)$, and the resonance frequency $\Omega_n = \pi v_w/(2\alpha L_n)$. Note that $\beta/\omega \cong \eta \ll 1$. From Eq. (S4), the surface response of a single FP resonator, i.e., the Green function, can be explicitly written as

$$G_n = \sum_{m=1}^{\infty}\frac{\chi_n}{(2m-1)^2\Omega_n^2 - \omega^2 - i\beta\omega}. \tag{S5}$$

In the vicinity of the first FP resonator (m=1), Eq. (S5) can be approximated as

$$G_n \cong \frac{\chi_n}{\Omega_n^2 - \omega^2 - i\beta\omega}, \tag{S6}$$

which is the origin of Eq. (4) plotted in Fig. 1(c-d) in the main text. For this step, we have ignored all the higher-order FP resonances within a single resonator and the approximation is valid around the first-order resonance Ω_n, where the contributions of the higher-order terms are negligible.

Text S2. Measurement of the loss factor

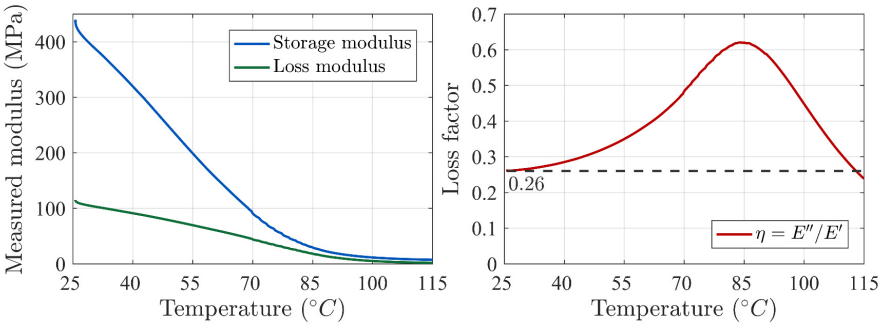

Fig. S1 **Measured results for the dynamic mechanical analysis.** (a) The storage modulus and the loss modulus, plotted as functions of temperature. (b) The loss factor, plotted as a function of temperature. The dashed line indicates the loss factor at room temperature.

The dynamic mechanical analysis (DMA) was carried out to characterize the loss factor of the composite materials. A sinusoidal stress was applied and the strain in the material is measured, allowing one to determine the complex modulus. The Young's modulus of the viscoelastic materials is defined by $E = E' - iE'' = E_c(1 - i\eta)$, where E' and E'' denote the storage modulus and loss modulus, respectively and the loss factor $\eta = E''/E'$. In Fig. S1(a), the real part of the modulus, is noted to be slightly greater than the measured 0.37×10^9Pa, given by the tensile test (carried out in room temperature) in the main text. Here, what we care about is the loss factor. Due to the inherent dispersive features of the relaxation mechanisms, the real and imaginary parts of the modulus can be a function of frequency. For simplicity, in the theoretical derivation and simulations, we adopt the value of 0.26 for η [Fig. S1(b)]. In the following section, we will also show that, due to the unique property of integrated Fabry-Perot resonators, the absorption performance is not sensitive to the loss factor.

Text S3. Integration scheme for multiple Fabry-Perot resonators

The overall impedance is given by the parallel superposition of surface responses from all the N composite FP resonator rods:

$$Z_s = \left(\frac{1}{N} \sum_{n=1}^{N} \frac{1}{Z_n} \right)^{-1} = -\frac{1}{i\omega} \left(\frac{1}{N} \sum_{n=1}^{N} G_n \right)^{-1} \cong -\frac{1}{i\omega} \left(\frac{1}{N} \sum_{n=1}^{N} \sum_{m=1}^{\infty} \frac{\chi_n}{(2m-1)^2 \Omega_n^2 - \omega^2 - i\beta\omega} \right)^{-1}. \quad \text{(S7)}$$

For simplicity, in Eq. (S7) we have assumed that the neighbouring FP resonators are separated by very small gaps with negligible surface area facing the incident wave. The factor $1/N$ accounts for the area fraction of each resonator facing the incident wave.

By treating the distribution of the resonance frequencies $(\Omega_1, \Omega_2, \ldots, \Omega_N)$ to be continuous, the discretized summation in Eq. (S7) can be rewritten as an integral:

$$Z_s = -\frac{1}{i\omega}\left(\frac{1}{N}\int_{\Omega_1}^{\infty}\sum_{m=1}^{\infty}\frac{\chi(\Omega)D(\Omega)}{(2m-1)^2\Omega^2-\omega^2-i\beta\omega}d\Omega\right)^{-1}, \tag{S8}$$

where the mode density $D(\Omega) = dN/d\Omega$ and the oscillation strength $\chi(\Omega) = 2/(\alpha\rho_w L_n) = 4\Omega/(\pi Z_w)$. The definition of Dirac delta function is $\delta(x) = \epsilon/[\pi(\epsilon^2 + x^2)]$ $(\epsilon \to 0)$ and here we have the dissipation β/ω much smaller than unity. Therefore, we can divide Eq. (S8) into real and imaginary parts:

$$Z_s^{-1} = -\frac{i\omega}{N}P\int_{\Omega_1}^{\infty}\sum_{m=1}^{\infty}\frac{\chi(\Omega)D(\Omega)}{(2m-1)^2\Omega^2-\omega^2}d\Omega + \frac{\pi\omega}{N}\int_{\Omega_1}^{\infty}\sum_{m=1}^{\infty}\chi(\Omega)D(\Omega)\delta\left[(2m-1)^2\Omega^2-\omega^2\right]d\Omega. \tag{S9}$$

The principal value of the first term in Eq. (S9) can be approximately treated as zero due to its oscillating characteristic. For the second term, we can perform the integration by utilizing the property of the delta function. So, by using the definition of the oscillation strength, Eq. (S9) may be simplified as

$$Z_s^{-1} = \frac{\pi}{2N}\sum_{m=1}^{\infty}\frac{\chi(\Omega)D(\Omega)}{2m-1}\bigg|_{\Omega=\frac{\omega}{2m-1}} = \frac{1}{Z_w}\sum_{m=1}^{\infty}\frac{2\Omega}{N}\frac{D(\Omega)}{2m-1}\bigg|_{\Omega=\frac{\omega}{2m-1}}. \tag{S10}$$

According to our impedance matching target of $Z_s(\omega) = Z_w$, Eq. (S10) can be rewritten as

$$\sum_{m=1}^{\infty}2\Omega\frac{d\tilde{n}/d\Omega}{2m-1}\bigg|_{\Omega=\frac{\omega}{2m-1}} = 1, \tag{S11}$$

where $d\tilde{n} = dN/N$ and $\tilde{n} \in [0,1]$. For convenience, we denote $a(\omega/(2m-1)) = 2\Omega d\tilde{n}/d\Omega$. By using this notation, Eq. (S11) becomes

$$a(\omega) + \frac{1}{3}a\left(\frac{\omega}{3}\right) + \frac{1}{5}a\left(\frac{\omega}{5}\right) + \ldots = 1. \tag{S12}$$

Below the cut-off frequency $(\omega/(2m-1) < \Omega_1)$, the mode density is zero, serving as the initial condition. So, we can calculate $a(\omega)$ by iterations based on the different frequency ranges and solve the ordinary differential equation with different a_m for each m. As the first step, if $\omega \in [\Omega_1, 3\Omega_1]$, only the first term survives due to the initial condition (i.e., $a(\omega) = a_1 = 1$). For the second step, if $\omega \in [3\Omega_1, 5\Omega_1]$, only the first and the second terms have nonzero values. So, $a(\omega) + a(\omega/3)/3 = a_2 + a_1/3 = 1$ and we can solve for $a_2 = 2/3$. By repeating the iteration procedures, we can solve for a_m for $\omega \in [(2m-1)\Omega_1, (2m+1)\Omega_1]$. The results are plotted in Fig. S2.

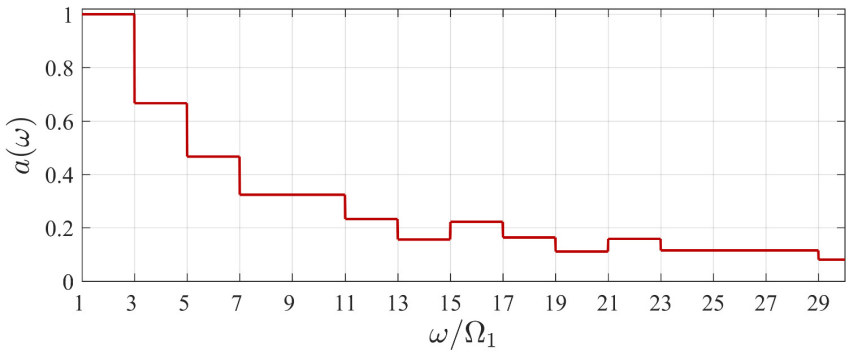

Fig. S2 **Iterated solution for the series coefficient $a(\omega)$.** The value of $a(\omega)$ is a constant within the frequency range $\omega \in [(2m-1)\Omega_1, (2m+1)\Omega_1]$. The solution curve shows that if $\omega \to \infty$, $a(\omega) \to 0$.

The physical meaning of a_m is that it can determine the mode density in the specified frequency range (i.e., $2\Omega d\tilde{n}/d\Omega = a_m$). For $m = 1$, we have $2\Omega d\tilde{n}/d\Omega = 1$ which has been derived in the main text with first-order approximation and the solution $\ln(\Omega/\Omega_1) = 2\tilde{n}/a_1$ for $\tilde{n} < \ln(3)/2$. By adopting the value of a_2, we can continue to obtain $\ln(\Omega/(3\Omega_1)) = 2(\tilde{n} - \ln(3)/2)/a_2$. We can repeat the procedure and obtain the complete information of Ω as function of $\tilde{n}$ [see the red solid line in Fig. 3(c) in the main text]. In the practical case, we can only have a finite number of FP resonators, so the distribution of the resonances Ω cannot be continuous as we have assumed. In the present case, we choose $N = 9$. The resulting distribution of the discretized first-order resonances $(\Omega_1, \Omega_2, \ldots, \Omega_N)$ is highlighted by the circles in Fig. 3(c) of the main text. In this manner, the length of the individual FP resonator rods can be determined as $L_n = \pi v_w/(2\alpha\Omega_n)$.

Text S4. Procedure for the fabrication of composite rods

In this section, we describe how the composite FP resonator rods were fabricated. In the last section, we have derived the lengths for the FP resonator rods. Accordingly, we prepare hard molds by 3D printing (the translucent one in step 2 of Fig. S3), with the dimensions of their protrusions the same as the required rods. By using the hard molds, we can use mold silica gel to fabricate the soft molds (the pink block in step 3 of Fig. S3).

Below are the detailed steps. (1) Uniformly mixing the original agent and curing agent for the mold material—silica gel. (2) Pouring the mixture into a hard mold made of acrylic. (3) After curing for 24 hours, the soft mold can be obtained by demolding. (4) Weighing the required tungsten powder. (5) Weighing the agent and the curing agent for rubber and resin, respectively. (6) Mixing these four polymers evenly, according to the pre-determined ratio. (7) Uniformly mixing the tungsten powder into the prepared polymer mixture. (8) Pouring the mixture into the soft mold. (9) After curing for about 12 hours, the solidified FP rods can be obtained by demolding. In this manner, 9 types of solid FP rod with different lengths can be obtained by reproducing different sizes of the soft molds.

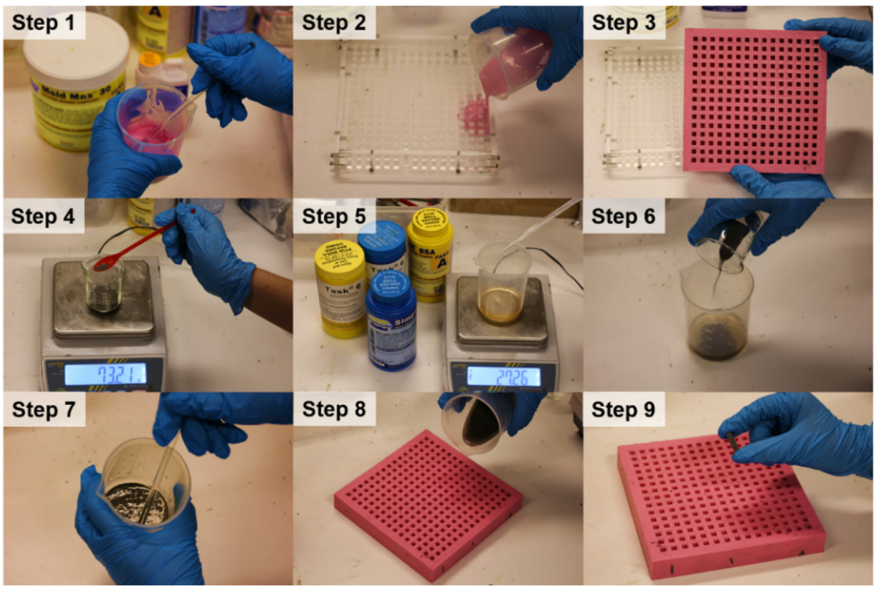

Fig. S3 **Steps for fabricating the composite rods.**

Text S5. Oblique incidence performance and the lateral size effect

In the main text, due to the limitation of the experiment, we only present the absorption under normal incidence. However, in practical situations waves impinge from all possible directions in the underwater environment. By using numerical simulations, we can examine the absorption in broader frequency range and under wider incident angles, and also deliberately tune the size of the lateral size of each rod. Here, we display the results in two groups. One is for the lateral size 5 mm (used in the main text) and the other is only $1/3$ of 5 mm. The simulated absorption results under various incident angles are presented in Fig. S4(a) and Fig. S4(b), respectively, for lateral sizes of 5 mm and 5/3 mm.

It turns out that for normal incidence, the reduction of the lateral size can enhance the higher frequency absorption beyond 20 kHz [see the comparison between the black lines in Fig. S4(a) and Fig. S4(b)]. This is due to the suppression of the lateral surface modes, which are in the form of evanescent waves in the incident wave direction with a decreased exponential decaying length when the lateral size of the rods is decreased. For oblique incidence, there can be similar effects in improving the higher frequency absorption. As for the data in Fig. S4(a), the high absorption remains to be above 90%, even with an oblique incident angle of 45 degrees. Even at a very large angle of 75 degrees, the absorption can be more than 60% over a broad frequency range. Therefore, the simulation study shows that decreasing the lateral size can have merits such as broader working frequency range for both normal and oblique incidence. However, smaller the lateral size of the rods, more rods would need to be fabricated so as to reach the pre-determined size of 0.92 m by 0.92 m. This is the reason why we chose 5 mm so as to strike a balance between the heavy

workload and the performance. For larger-scale applications, automated machine production in the future can certainly adopt the smaller lateral sizes. It should also be noted that composite material's high index of refraction can mean that even for oblique incidence, the refracted wave inside the composite is largely longitudinal.

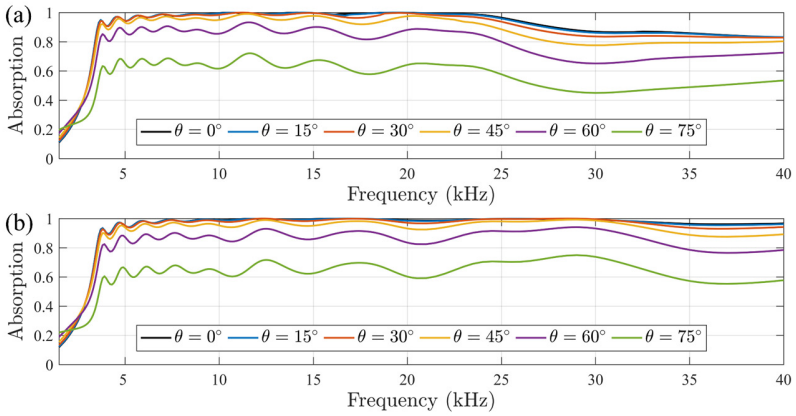

Fig. S4 **Oblique incidence performance.** (a) Results for the 5 mm lateral rod size. (b) Results for the lateral size of $5/3$ mm.

Text S6. Performance under the hydrostatic pressure

An ideal hydroacoustic absorber should be able to maintain its performance even in the presence of a certain hydrostatic pressure. We use simulations to explore the possibility of acoustic absorption under the hydrostatic pressure with a water depth of $H = 500$ m, which means the upper surface of the absorber is under the pressure $p_0 = \rho_0 g H = 5 \times 10^6$Pa ($g = 10$ m/s^2). In the relevant simulation, we considered the deformation of the absorber. In particular, the four sides around the rods will bulge and the length of the rods will be slightly decreased [see the inset in Fig. S5]. In simulation, we have taken nonlinearity caused by the deformation into consideration, by enabling 'nonlinearity' option in COMSOL Multiphysics. Also, we can evaluate the displacement of the sides and the outcome value is around 15 μm, which is smaller than the predesigned air gap width (50 μm). The actual situation should be that the rods may have some point contacts, since the side surfaces cannot be atomically smooth, but this will not dramatically affect the longitudinal modes.

As long as the air gaps exist and be well sealed inside the sample, the longitudinal modulus should be close to the Young's modulus, which is the premise of our absorption mechanism. In fact, it is well-known that the air bubbles dispersed in the fluid can significantly change their compressibility characteristics. In contrast to air-bubble-based absorbers, where the bubble deformation can be very significant under large hydrostatic pressure so that the original absorption modes may deviate from the pre-designed ones, for our integrated Fabry-Perot absorber the hydrostatic pressure can only have very limited effect on its absorption performance. This is

evident from the comparison between the dashed grey line and red line in Fig. S5. Although only experiments can fully verify the performance under high water pressure, in principle, our design is theoretically self-consistent and can be a potential candidate for mitigating the performance-degrading problem under elevated pressure.

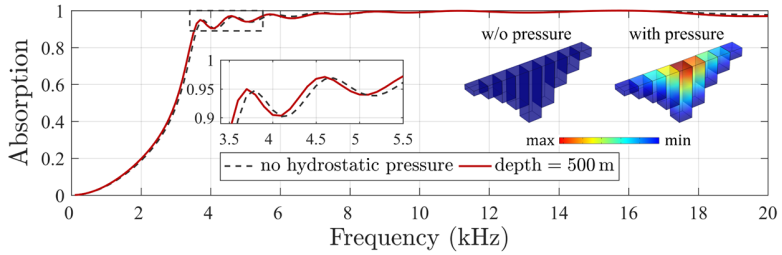

Fig. S5 **Absorption spectra with and without the hydrostatic pressure.** The inset figure on the left gives an enlarged view showing the deformation effect of the composite rods. The two figures on the right show, with color, the magnitude of the displacement caused by pressure (blue is zero and red is the maximum).

Text S7. Tunability of the absorption band

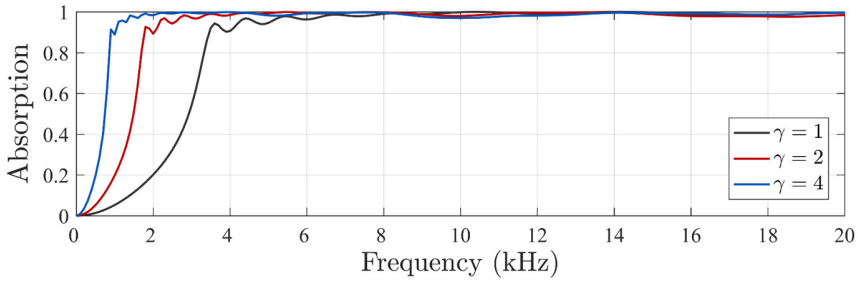

Fig. S6 **Absorption spectra under different scaling factor γ.**

A useful feature of our work is that the modes can be designed by only varying the length of the rods. In the present work we have fixed the initial resonance frequency to be around 3.5 kHz. In this section, we show that the absorbing bands can be easily tuned, by introducing a scaling factor to the original length recipe $(L_1, L_2, \dots, L_9)$. Namely, the updated lengths should be $(\gamma L_1, \gamma L_2, \dots, \gamma L_9)$ and the lateral dimensions remain unchanged. In this manner, we can change the lower cut-off frequency of the absorption spectrum from f_1 to f_1/γ. In other words, we use more thickness for lower frequency absorption performance by lengthening original averaged length from $\bar{d}$ to be $\gamma\bar{d}$. In Fig. S6, the simulation results show that the absorption bands are shifted down to 2 kHz and 1 kHz with $\gamma = 2$ and 4, respectively, without losing the absorption performance at higher frequencies. If the target frequency range or the allowed thickness are changed, in the present sample design we only have to simply scale the length of the FP resonator rods.